

Aggregation Kinetics of Polysorbate 80/*m*-Cresol Solutions: A Small-Angle Neutron Scattering Study

Peter H. Gilbert, Zhenhuan Zhang, Ken K. Qian,* David P. Allen, Rachel Ford, Norman J. Wagner,* and Yun Liu*



Cite This: *Mol. Pharmaceutics* 2022, 19, 862–875



Read Online

ACCESS |



Metrics & More

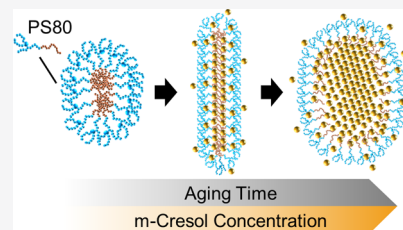


Article Recommendations



Supporting Information

ABSTRACT: Polysorbate 80 (PS80), a nonionic surfactant used in pharmaceutical formulation, is known to be incompatible with *m*-cresol, an antimicrobial agent for multi-dose injectable formulations. This incompatibility results in increased turbidity caused by micelle aggregation progressing over weeks or longer, where storage temperature, ionic strength, and component concentration influence the aggregation kinetics. Small-angle neutron scattering (SANS) analysis of PS80/*m*-cresol solutions over a pharmaceutically relevant concentration range of each component reveals the cause of aggregation, the coalescence mechanism, and aggregate structure. PS80 solutions containing *m*-cresol concentrations below ≈ 2.0 mg/mL and above ≈ 4.5 mg/mL are kinetically stable and do not aggregate over a 50 h period. At 5 mg/mL of *m*-cresol, the mixture forms a kinetically stable microemulsion phase, despite being well below the aqueous solubility limit of *m*-cresol. Solutions containing intermediate *m*-cresol concentrations (2.0–4.5 mg/mL) are unstable, resulting in aggregation, coalescence, and eventual phase separation. In unstable solutions, two stages of aggregate growth (nucleation and power-law growth) are observed at *m*-cresol concentrations at or below ≈ 3.6 mg/mL. At higher *m*-cresol concentrations, aggregates experience a third stage of exponential growth. A single kinetic model is developed to explain the stages of aggregate growth observed in both kinetic mechanisms. This work establishes the phase diagram of PS80/*m*-cresol solution stability and identifies component concentrations necessary for producing stable formulations.



KEYWORDS: micelles, small-angle neutron scattering, polysorbate, preservatives, pharmaceutical formulation

1. INTRODUCTION

Surfactants are commonly included in many pharmaceutical products, such as monoclonal antibody formulations¹ and fusion protein solutions.^{2,3} They prolong storage lifetimes and improve drug safety profiles by coating vial walls and associating with the therapeutic protein.⁴ Surfactants can prevent protein aggregation and partial unfolding arising from protein–protein interactions and protein–surface adsorption.^{5–9} The resulting stable formulation should be free of turbidity.¹⁰

Polysorbate 80 (PS80), or polyoxyethylene (20) sorbitan monooleate, is a common surfactant used in formulation.^{1–3,5–10} PS80 is amphiphilic, consisting of a hydrophilic polyoxyethylene head group of approximately 20 monomeric units^{11,12} attached by an ester bond to a hydrophobic oleic acid tail. Though the molecule containing a single oleic acid tail is the most common variant in commercially available PS80, PS80 is usually a mixture containing pairings of several different fatty acid tails, including species having multiple tails attached to a single head group.⁷ This heterogeneity of polysorbates is integral to their performance in solution stabilization but can lead to variable performance between manufactured polysorbate batches.¹¹

An anti-microbial preservative can be included in multi-dose formulations to ensure consumer safety.⁶ Small organic

preservatives, such as phenol and 3-methyl phenol (or *m*-cresol), are often used in multi-dose injectable pharmaceutical formulations at concentrations around 3 mg/mL.¹³ Compared with phenol, *m*-cresol shows slightly improved antimicrobial activity and has fewer known incompatibilities with other excipients. However, it is well documented that the *m*-cresol activity is reduced by the presence of nonionic surfactants, including polysorbates.^{6,14} The source of incompatibility between these common pharmaceutical excipients is not well understood.⁶

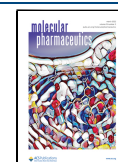
Above its critical micelle concentration (CMC) or CMC range (CMR),^{15,16} PS80 in aqueous solution is known to self-assemble into ellipsoidal core–shell micelles (see Figure 1 of refs 7 and 117). Micelles formed by either all-oleate PS80 or commercial grade PS80 are suitably described by core–shell ellipsoid models.^{7,17} A small-angle neutron scattering (SANS) study found that core–shell ellipsoid modeling was also suitable for another polysorbate surfactant, PS20, even when it

Received: October 21, 2021

Revised: January 20, 2022

Accepted: January 20, 2022

Published: February 9, 2022



was mixed with an anionic surfactant.¹⁸ PS80 micelles have a radius of gyration (R_g) of $\approx 3.0 \pm 0.1$ nm in water at 22 °C^{7,17} and a hydrodynamic radius (R_H) of ≈ 4.0 nm in water to 5 nm in buffered water at 25 °C.^{9,15,16} Addition of small organic excipients, such as 1,4-dioxane¹⁹ or dimethyl sulfoxide,²⁰ to solutions of PS80 alters the micelle morphology. However, PS80 micelles were unaffected by increasing *N,N*-dimethylformamide concentration.²¹ Micelles in 150 mg/mL PS80 solutions swell when 50 mg/mL of dimethyl trisulfide is added, where only approximate micelle sizes were extracted from cryo-transmission electron microscopy.²² Recent work has shown that after adding polysorbates to 2.8 mg/mL *m*-cresol solutions, the samples remain transparent up to a critical PS80 concentration of ≈ 0.02 mg/mL.⁶ Above this PS80 concentration, all solutions had increased turbidity caused by aggregate formation. Shi et al. also discovered that the PS80 concentration in these turbid solutions decreased over a 28 day period,⁶ suggesting the important role of aggregation in solution instability.

Recent SANS work has revealed that previously observed changes in turbidity were caused by the continuous coalescence of PS80/*m*-cresol micelles into large droplets over the course of months.¹⁷ The aggregation kinetics were described by a two-stage process, where the first stage of initial growth was followed by a period of coalescence corresponding to diffusion-limited aggregation, where increasing aggregate size had a power-law dependence on time. The initial growth stage was proposed to correspond to incorporation of *m*-cresol into or rearrangement of PS80 micelles. Coalescence of PS80/*m*-cresol aggregates after the initial rearrangement period produced a narrow size distribution of larger aggregates, where the size distribution did not broaden with time. Increasing temperature caused acceleration of aggregate growth that obeyed time–temperature superposition, where higher temperatures can be used to explore longer aggregation times. The addition of a citrate buffer to PS80/*m*-cresol solutions also accelerated the coalescence mechanism and caused total phase separation of a few large oily droplets from the surrounding aqueous phase within days.¹⁷ We expand on this SANS study by determining the influence of component concentration on the mechanism and growth kinetics of PS80/*m*-cresol aggregates and provide further insight into aggregate morphology. Additionally, we develop a phase diagram of incompatibility over the pharmaceutically relevant concentration range.

Current pharmacopeias place limits on particle size and loading in parenteral therapeutics and limit uncontrolled aggregate formation. USP <787>, USP <788>, and Ph. Eur. 2.9.19 detail the use of optical or light obscuring techniques for analysis of particle size in parenteral solutions. Though turbidity and light scattering measurements provide information on particle size distribution, they are limited to studying a narrow range of particle sizes compared to other scattering techniques. Here, we use SANS to examine the effect of *m*-cresol and PS80 concentrations on time-dependent aggregate growth. SANS is a powerful technique to probe nanoscale structure and composition at relevant excipient concentrations and physicochemical conditions.^{7,17,23} From the measured scattering curves, we extract the aggregation kinetics, growth mechanism, and aggregate morphology. We complete our study by producing a phase diagram of PS80/*m*-cresol solution stability and provide a working model of aggregation kinetics.

2. METHODS

2.1. Materials. PS80 and 99% *m*-cresol were obtained from Sigma-Aldrich (St. Louis, MO). 99% deuterium oxide (D_2O) was purchased from Cambridge Isotope (MA). PS80 was stored at 4 °C, while *m*-cresol was stored at 22 °C.

2.2. Sample Preparation. Diluted stock solutions of ≈ 4.5 mg/mL PS80 in D_2O were prepared from stock PS80 and used for mixture formulation. Similarly, ≈ 7.2 mg/mL *m*-cresol solutions were prepared by dissolving *m*-cresol in D_2O . All subsequent solutions were prepared by combining these stock PS80 and *m*-cresol solutions. Specifically, solutions containing 0.2–1 mg/mL PS80 and 1.0, 1.5, 2.0, 2.6, 3.15, 3.6, 4.0, 4.5, or 5.0 mg/mL *m*-cresol were used to study a range of pharmaceutically relevant component concentrations. The surfactant concentrations explored in this study are approximately 10 \times the CMC of PS80 (0.02–0.04 mg/mL) over the entire experimental temperature range of 4–37 °C, where higher temperatures correspond to lower CMCs.^{16,24} A more recent study using surface tension measurements has found that there is no clear PS80 CMC value. Instead, there is a CMR of ≈ 0.01 – 0.02 mg/mL at 25 °C because PS80 is a mixture of chemical species.^{15,16} The solubility limit of *m*-cresol in water is 22.7 mg/mL at 25 °C,²⁵ well above the concentrations used in this study.

All samples were prepared at ≈ 22 °C and immediately brought to measurement temperature through Peltier cooling or heating in the sample chamber. Each sample was briefly mixed by hand through shaking before injection into sample cells, which were subsequently placed in a temperature-controlled sample chamber.

When using D_2O as the solvent, the contrast between PS80 and D_2O is almost the same as the contrast between *m*-cresol and D_2O because the scattering length densities (SLDs) of PS80 and *m*-cresol are more similar to each other than they are to D_2O ($SLD_{PS80} = 0.549 \times 10^{-6} \text{ \AA}^{-2}$; $SLD_{m\text{-cresol}} = 1.398 \times 10^{-6} \text{ \AA}^{-2}$; $SLD_{D_2O} = 6.33 \times 10^{-6} \text{ \AA}^{-2}$). This suggests a simplified effective two-component analysis of the aggregate nanostructures, where *m*-cresol and PS80 are one phase and D_2O the second. This simplification is integral to the scattering invariant analysis.

2.3. SANS Techniques and Modeling. Measurements were performed on the very-small-angle neutron scattering (vSANS) and the NGB30m SANS beam lines at the National Institute of Standards and Technology (NIST) Center for Neutron Research (NCNR) in Gaithersburg, MD. Solutions of PS80 without *m*-cresol were analyzed using the NGB30m SANS at detector distances of 1 m ($q \approx 0.06$ – 0.5 \AA^{-1} ; 6 \AA neutrons) and 4 m ($q \approx 0.01$ – 0.1 \AA^{-1} ; 6 \AA neutrons) with 600 and 1000 s collection times. The scattering curves of *m*-cresol containing PS80 solutions without buffering were collected using vSANS at all temperatures (4, 22, and 37 °C) for the front ($q \approx 0.03$ – 0.2 \AA^{-1}) and middle ($q \approx 0.002$ – 0.04 \AA^{-1}) detectors at 4.6 and 18 m using 6 \AA neutrons and 900–1800 s collection times, where count times increased as the samples aged. Titanium sample cells were 2 mm in thickness with quartz windows for all measurements. The samples were gently loaded into cells using a syringe.

Data reduction, Guinier analyses, and Porod analyses for all sample scattering were completed in Igor Pro 8.04 64-bit by WaveMetrics, Inc.²⁶ SasView 5.0.3 (www.sasview.org/), an open-source scattering analysis software, was used for scattering curve model fitting and scattering invariant

calculations.²⁷ All analysis was carried out on Microsoft Windows 10 Home 64-bit.

2.4. SANS Aggregation Analysis. This section summarizes the SANS analyses applied to characterize the PS80/*m*-cresol aggregate morphology and growth. By examining the intensity of scattered neutrons, the radius of gyration (R_g), aggregation number (N_{Agg}), aggregate surface area (S), and, when examined over time, changes in micelle composition can be determined.^{28–30} Generally, for systems consisting of monodispersed spherical particles, the absolute scattering intensity, $I(q)$, is

$$I(q) = \phi(\Delta\rho)^2 V_p P(q) S(q) + B \quad (1)$$

where ϕ is particle volume fraction, $\Delta\rho$ is the contrast, $V_p = N_{\text{Agg}} V_{\text{mol}}$ is particle volume, $P(q)$ is the normalized form factor describing micelle shape, $S(q)$ is the inter-particle structure factor, V_{mol} is the molecular volume, and B is the background. Tables S1 and S2 in the Supporting Information summarize the dimensional and dimensionless material properties. Equation 1 can be readily generalized to polydisperse suspensions as well as some nonspherical particles, and such models are incorporated into modern data analysis programs, such as SasView, which is used here. The magnitude of the scattering vector, q , is (see eq 3.7 of ref 28)

$$q = \frac{4\pi \sin \frac{\theta}{2}}{\lambda} \quad (2)$$

where θ is the angle between incident and scattered wave vectors and λ is the neutron wavelength.

For a dilute solution ($S(q) \approx 1$) and low- q , the Guinier approximation can be used for the normalized form factor

$$P(q) = e^{-1/3 q^2 R_g^2}; \quad q R_g \ll 1 \quad (3)$$

so that

$$\ln(I(q) - B) = \ln(\phi(\Delta\rho)^2 V_p) - \frac{1}{3} q^2 R_g^2 \quad (4)$$

which relates $I(q)$ and R_g and is model independent. Taking the limit yields

$$\lim_{q \rightarrow 0} I(q) - B = I_0 = \phi(\Delta\rho)^2 V_p \quad (5)$$

where the aggregate volume, V_p , is proportional to the zero- q intensity, I_0 , for constant ϕ and contrast or SLD difference, $\Delta\rho$, which is reasonable for PS80/*m*-cresol solutions. For solutions containing only PS80, the average number of PS80 molecules participating in each micelle, N_{Agg} , can be estimated using $N_{\text{Agg}} = V_p/V_{\text{mol}}$. In mixed PS80/*m*-cresol solutions, N_{Agg} for PS80 is instead estimated from the mass balance along with the micelle core SLD, ρ_c , and volume fitted using the scattering data

$$N_{\text{Agg,PS}} = \frac{\rho_c - \phi_{\text{mc,c}} \rho_{\text{mc}}}{V_{\text{mol,o}} \rho_o} V_c \quad (6)$$

where $\phi_{\text{mc,c}}$ is the *m*-cresol volume fraction in the core, ρ_{mc} is the SLD of *m*-cresol, V_c is the core volume, $V_{\text{mol,o}}$ is the volume of an oleic acid tail, and ρ_o is the SLD of an oleic acid tail. Equation 6 assumes that no D₂O inhabits the hydrophobic micelle core. Estimates of aggregation number for each scattering measurement are reported along with the model fit parameters in Tables S3 and S4.

Changes in aggregate composition with time can be detected using the two-component scattering invariant, Q^*

$$Q^* \equiv \int_0^\infty q^2 (I(q) - B) dq = 2\pi^2 (\Delta\rho)^2 \phi(1 - \phi) \quad (7)$$

where the last equality is for homogeneous particles in a homogeneous solvent. The invariant is an estimate of the total scattering intensity for a material, which is conserved if the material composition, ($\Delta\rho$), and volume fraction, ϕ , remain unchanged. In other words, if the invariant is constant with time, the aggregate composition also remains constant despite changes in aggregate size.

A core–shell ellipsoid model is used to estimate the size and structure of PS80/*m*-cresol micelles and aggregates. This model assumes that micelles consist of a core surrounded by a shell having a different SLD and allows the thickness and aspect ratio of these two domains to vary. Core and shell SLDs were also allowed to vary during fitting. A mass balance of PS80, *m*-cresol, and D₂O was used to constrain SLD fits, as they reflect the approximate volume fraction of each component in the core and shell. Domain sizes were also constrained by a molecular balance on PS80, where the number of heads in the shell matched the number of tails in the core. The primary advantage of the core–shell ellipsoid model is its flexibility for fitting a diverse range of micelle morphologies. Size polydispersity is also introduced to determine the size distribution of the coalescing aggregates. The fitting parameters and theoretical details for this model are laid out on the SasView 5.0.3 documentation page.³¹

2.5. Modeling Aggregate Growth. Model fits of PS80/*m*-cresol solution aggregation kinetics were previously limited to the power-law regime that dominates at long times¹⁷

$$R_g(t) = A \left(\frac{t}{a} \right)^{1/d_f} \quad (8)$$

where A is a scaling coefficient, a is the shift factor, and d_f is the fractal dimension. Equation 8 derives from diffusion-limited colloid aggregation (DLCA) theory, where a in eq 8 is related to t_p of DLCA theory (see eq 7 of refs 32 and 33). The shift factor, a , is a function of component concentration and temperature, where its temperature dependence, a_T , follows an Arrhenius–WLF relation (see eq 8 of ref 17)

$$\log a_T = \frac{-C_1(T - T_0)}{C_2 + (T - T_0)} \quad (9)$$

For $R_g(t)$ data, the best fits for constants C_1 and C_2 are 3.83 and 85.0 K and $T_0 = 295$ K. A similar function is found for the concentration dependence of a

$$\log a_c = \frac{-C_{1,c}(c_{\text{mc}} - c_{\text{mc},0})}{C_{2,c} + (c_{\text{mc}} - c_{\text{mc},0})} \quad (10)$$

where $C_{1,c} = 0.82$, $C_{2,c} = 2.0$ mg/mL, $c_{\text{mc},0} = 3.15$ mg/mL are the best fits with $\chi^2 = 0.02$ and c_{mc} is the *m*-cresol concentration. Equation 10 is valid for $k_1 = \infty$, when 2.0 mg/mL $\leq c_{\text{mc}} \leq 3.6$ mg/mL. The total shift factor is the product a_T and a_c , such that $a \equiv a_T a_c$. These shift factors allow the power-law regions of $R_g(t)$ data to be collapsed onto a single master curve, making time–temperature superposition possible.

Equation 8 describes the power-law coalescence observed at long times without considering the early nucleation and

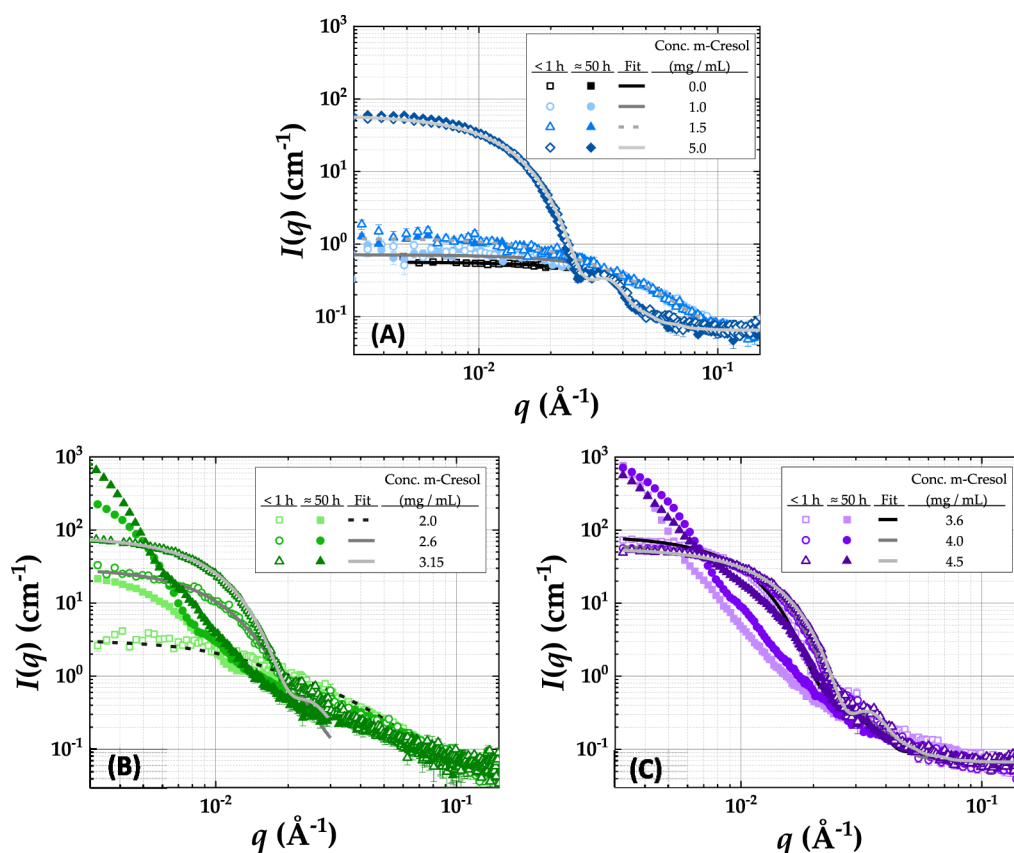


Figure 1. $I(q)$ (cm^{-1}) vs q (\AA^{-1}) plots of unbuffered 1.0 mg/mL PS80 solutions with 0.0–5.0 mg/mL *m*-cresol that are (A) stable, (B) type I unstable, and (C) type II unstable at $T = 22$ °C for growth times of <1 h ($\square\circ\triangle\diamond$) and ≈ 50 h ($\blacksquare\bullet\blacktriangle\blacklozenge$) with core-shell ellipsoid (—) and core-shell cylinder (---) model fits. The fit parameters are detailed in Tables S3 and S4 of the Supporting Information. The error bars represent 1 standard deviation and are often smaller than the plot symbols.

exponential growth stages observed for some cases in this study. To accommodate these mechanisms, an exponential growth term, associated with reaction-limited colloidal aggregation (RLCA),³⁴ replaces A in eq 8 to get

$$R_g(t) = A_R \left(\frac{t}{a} \right)^{1/d_f} \left(1 - \frac{k_2[A]_0 + k_1}{k_2[A]_0 + k_1 e^{(k_2[A]_0 + k_1)t/a}} \right) + R_g(0) \quad (11)$$

where $R_g(0)$ is the radius of gyration at $t = 0$, k_1 and k_2 are the aggregation rate constants representing the energy barrier for aggregate coalescence, $[A]_0$ is the initial micelle concentration, and A_R is a scaling factor. Equation 11 combines the kinetics for the diffusion-limited coalescence of eq 8 and the sigmoidal nucleation reaction having the form of a modified Finke–Watzky (F–W) two-step model.^{35–37} Equation 11 is derived in the Supporting Information. When aggregation is not limited by the reaction ($k_1 \rightarrow k_d$), eq 11 reduces to the special case of eq 8 at long times, where k_d is the diffusion-limited rate constant. At the opposite limit, the energy barrier to aggregation is insurmountable ($k_1 = 0$) such that eq 11 reduces to $R_g(t) = R_g(0)$. Thus, eq 11 can describe the micelle size in aggregating and stable PS80/*m*-cresol solutions.

Though eq 11 is written in terms of R_g , this combined mode aggregation equation can be reformulated for the zero- q scattering intensity, I_0 , so that

$$I_0(t) = A_I \left(\frac{t}{a_I} \right)^{1/d_I} \left(1 - \frac{k_2[A]_0 + k_1}{k_2[A]_0 + k_1 e^{(k_2[A]_0 + k_1)t/a_I}} \right) + I_0(0) \quad (12)$$

where A_I is a scaling coefficient, a_I is the shift factor, d_I is the inverse power-law coefficient, and $I_0(0)$ is the zero- q intensity at $t = 0$. These parameters are different from those introduced for the R_g model [eq 11] but have similar interpretations. The initial micelle concentration, $[A]_0$, is determined using

$$[A]_0 = \frac{\phi_A^2 (\Delta\rho)^2}{I_0(0) N_A} \quad (13)$$

where ϕ_A is the total micelle volume fraction, N_A is the Avogadro constant, and $\Delta\rho$ is the scattering contrast between micelles and solvent. $[A]_0$ and the rate coefficients, k_1 and k_2 , are the same for eqs 11 and 12. Thus, the reaction-limited features in eqs 11 and 12 depend on the component concentration and temperature but not on the type of analysis, R_g or I_0 .

3. RESULTS

In this section, SANS results and associated analyses for solutions containing 0.2–1 mg/mL PS80 and 1–5 mg/mL *m*-cresol in D_2O are used to understand the PS80/*m*-cresol solution instability. First, the model fits of time-dependent PS80/*m*-cresol aggregate morphology are discussed to provide insight into aggregate shape and size. Next, the effect of varying

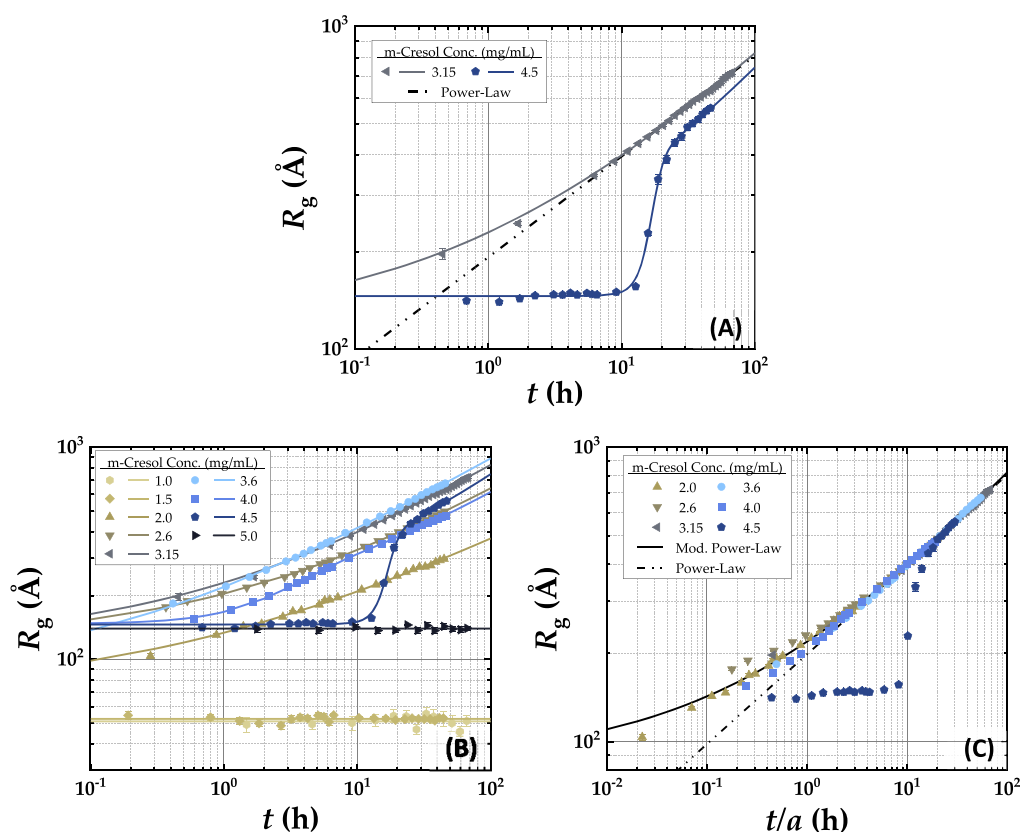


Figure 2. R_g (Å) plots of unbuffered 1.0 mg/mL PS80 solutions with 0–5.0 mg/mL *m*-cresol in D₂O at $T = 22$ °C showing (A) examples of type I (gray ◀) and type II (blue ◻) unstable aggregation vs t (h) along with kinetic model fits [eq 11] and a power-law fit [eq 8], (B) aggregation kinetics vs t (h) and kinetic model fits [eq 11] for 0–5.0 mg/mL *m*-cresol, and (C) time-shifted, t/a (h), master curve resulting from concentration-dependent shift factors, a , along with power-law [eq 8] and modified power-law [eq 11] fits ($k_1 \rightarrow k_d$), where shift factors are reported in Table S5 of the Supporting Information along with kinetic model fit parameters. The error bars represent 1 standard deviation.

component concentration on aggregate morphology and growth kinetics is examined. The discussion concludes with a solution stability phase diagram outlining the necessary conditions for PS80/*m*-cresol aggregation. This diagram also identifies solution conditions that generate stable formulations. The scope of this work is limited to concentrations within the typical formulation range of 1–5 mg/mL of *m*-cresol and 0.2–1 mg/mL of PS80.

Previous work only studied PS80/*m*-cresol solutions having a single *m*-cresol concentration (2.7⁶ or 3.15 mg/mL¹⁷). Here, the effect of varying *m*-cresol concentration from 0 to 5 mg/mL is addressed, where all solutions contain 1 mg/mL PS80. Specifically, this subsection focuses on changes in the aggregate morphology resulting from changes in the *m*-cresol concentration. The phase stability of these solutions can be divided into two groups for the ease of discussion: stable (no aggregation) and unstable (aggregation). In stable solutions, the micelle size remains unchanged over the experimental time frame, while unstable solutions show an increase in aggregate size with time. Here, stability classification is based on aggregation kinetics. Thus, “stable” solutions may be kinetically stable without being thermodynamically stable.

3.1. Morphology of Stable PS80/*m*-Cresol Solutions.

The SANS results for PS80/*m*-cresol solutions containing 0–5 mg/mL *m*-cresol with 1 mg/mL PS80 in D₂O are shown in Figure 1 along with the associated model fits. The model fit parameters are detailed in Tables S3 and S4 of the Supporting Information. The SANS intensity curves for the four PS80/*m*-

cresol solutions that are stable over a 50 h time frame are shown in Figure 1a. For both low (<2 mg/mL) and high (>4.5 mg/mL) concentrations of *m*-cresol, the intensity curves remain unchanged with time, where the early time results (<1 h) match those at longer times (≈ 50 h). Figures 2b and 3b also show the time-invariant size (R_g) and mass (I_0) for these stable solutions. Though all the curves in Figure 1a correspond to stable solution conditions, the micelle morphology differs between solutions having low (≤ 1.5 mg/mL) and high (5 mg/mL) *m*-cresol concentrations.

In the absence of *m*-cresol, PS80 micelle scattering can be fit by a core–shell ellipsoidal model. Previous work fit similar scattering measurements with oblate ellipsoidal micelles, where the ratio of the polar to equatorial core radii was $R_{c,pol}/R_{c,eq} \approx 0.5$.^{7,17} Prolate ellipsoids with $R_{c,pol}/R_{c,eq} \approx 2$ produce an equally good fit of our scattering data as oblate ellipsoids, when the micelle volume is kept constant. Here, the prolate ellipsoidal micelle model is favored because micelle elongation is observed with increasing *m*-cresol concentration. Stable micelles at 1.0 mg/mL *m*-cresol concentration are best represented as prolate core–shell ellipsoidal micelles having a polar to equatorial core radius ratio of $R_{c,pol}/R_{c,eq} \approx 4.3$, which is twice that of the 0 mg/mL *m*-cresol solution. This suggests that micelles accommodate the presence of *m*-cresol by elongating to maintain a stable morphology. The micelle volume in 1 mg/mL *m*-cresol solutions is 35% larger than in 0 mg/mL *m*-cresol solutions (Table S3). SLD analysis reveals that micelle swelling is caused by the incorporation of *m*-cresol

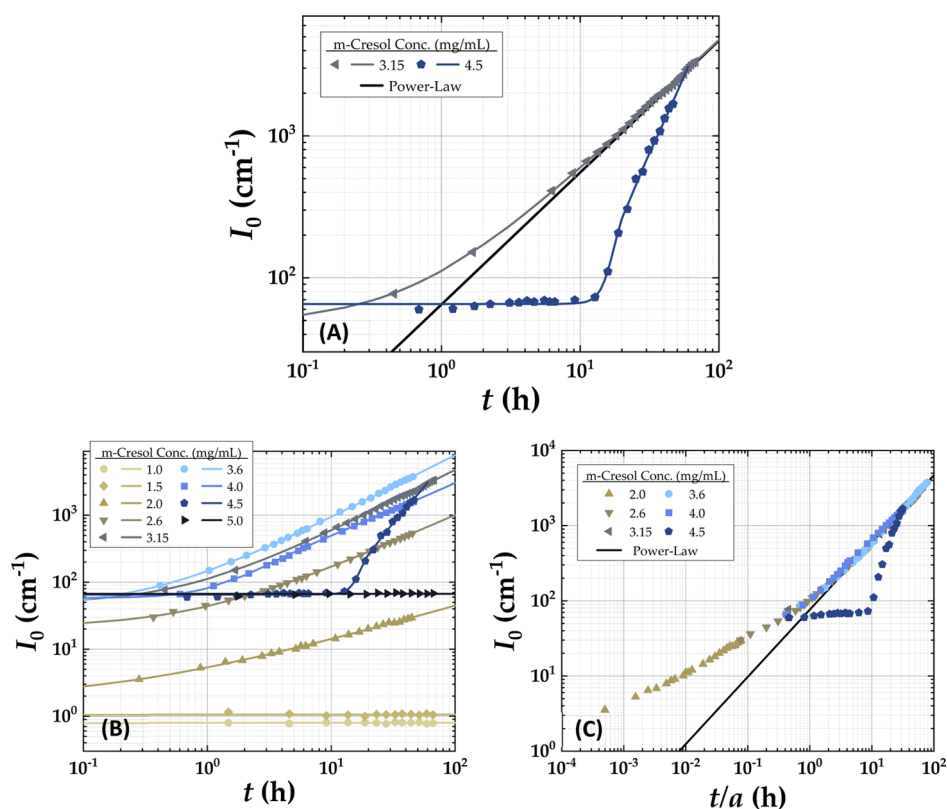


Figure 3. Low- q intensity, I_0 (cm^{-1}), plots of unbuffered 1.0 mg/mL PS80 solutions with 0–5.0 mg/mL m -cresol in D_2O at $T = 22$ °C showing (A) examples of type I (gray \blacktriangleleft) and type II (blue \circ) unstable aggregation vs t (h) along with kinetic model fits [eq. 12] as well as a power-law fit [eq. 8], (B) aggregation kinetics vs t (h) and kinetic model fits [eq. 12] for 0–5.0 mg/mL m -cresol, and (C) time-shifted, t/a (h), master curve resulting from concentration-dependent shift factors, a , along with a power-law fit [eq. 8], where shift factors are reported in Table S6 of the Supporting Information along with kinetic model fit parameters. The error bars represent 1 standard deviation.

at a total volume fraction of 0.16, where $\approx 66\%$ of m -cresol resides in the micelle core. This preference of m -cresol for the hydrophobic micelle core agrees with the partition coefficient for m -cresol of $\log P_{\text{oct/wat}} = 1.96$.³⁸ Figure S1 provides an illustrated approximation of stable micelle morphology without m -cresol, with low m -cresol concentrations, and with high m -cresol concentrations.

The scattering intensity curves for stable solutions containing 1.5 mg/mL m -cresol are best characterized with a core–shell cylinder model with $L/R \approx 8$ (Table S3). The micelle volume also doubles between 1.0 mg/mL m -cresol and 1.5 mg/mL m -cresol, further supporting the observation of m -cresol-induced swelling and elongation. These larger cylindrical micelles contain more D_2O in their shells, causing the m -cresol content to decrease to a total volume fraction of 0.06, where the core contains $\approx 75\%$ of m -cresol. Because 1.5 mg/mL m -cresol solutions are near the phase instability transition, the change in morphology and core composition may provide insight into the cause of aggregate formation. However, it is clear that m -cresol incorporation into micelles causes elongation meant to maintain stability.

At high m -cresol concentrations (5 mg/mL), the sample is also stable during our experimental time frame. Analysis indicates that the microemulsion droplets³⁹ in these solutions have a morphology that is more spherical ($R_{\text{c, pol}}/R_{\text{c, eq}} = 1.5$) than micelles in low-concentration solutions (< 1.5 mg/mL m -cresol). This is supported by the distinct intensity peak at $q = 3.2 \times 10^{-2} \text{ \AA}^{-1}$ in Figure 1a, which is a common feature in scattering curves for nearly spherical particles. These micro-

emulsion droplets are also much larger ($R_g = 140 \text{ \AA}$) than the micelles at low m -cresol concentrations ($R_g \approx 52 \text{ \AA}$), where Table S4 reports the radius of gyration calculated from the Guinier analysis for each solution. Model fits in Table S3 also show that droplets in 5 mg/mL m -cresol solutions have a volume that is 22 times larger than those in 1.5 mg/mL m -cresol solutions. The total volume fraction of m -cresol is 0.73, where 90% of m -cresol is in the core. This large amount of core m -cresol appears to require a more spherical micelle packing so that the microemulsion stability is maintained. PS80 is known to disperse antimicrobial agents with poor aqueous-phase solubility by producing a stable microemulsion.^{40,41} PS80/ m -cresol solutions experience a similar effect, where soluble m -cresol preferentially partitions into PS80 micelles to form the microemulsion.

Stable solutions have time-invariant mass-to-volume ratios (density), I_0/R_g^3 , as shown in Figure 4. This suggests that the micelle composition is constant with time. This is further supported by Figure S2, where the scattering invariant is also constant over time for these stable solutions. This confirms that the total volume fraction of micelles is time invariant.

The stability regimes for PS80/ m -cresol solutions over the m -cresol concentration range are identified in Figure 5 as a stability phase diagram. The solution stability for m -cresol concentrations below 2 mg/mL and at 5 mg/mL is represented by the unchanging R_g (Figure 5a) and I_0 (Figure 5b) over 50 h. Thus, the ratios of $R_g(50)/R_{g,i}$ (Figure 5c) and $I_0(50)/I_{0,i}$ (Figure 5d) are unity for these stable formulations. Though solutions containing low and high m -cresol concentrations are

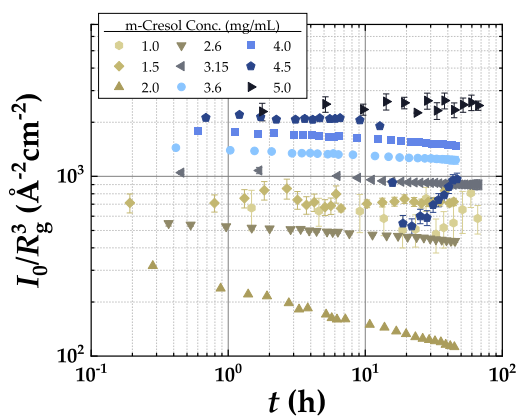


Figure 4. Aggregate density estimate, I_0/R_g^3 , vs t (h) for unbuffered 1.0 mg/mL PS80 solutions with 1.0–5.0 mg/mL m -cresol in D_2O at $T = 22$ °C showing time-invariant aggregate density at most m -cresol concentrations and the general increase in aggregate density with higher m -cresol concentrations. The error bars represent 1 standard deviation and are often smaller than the plot symbols.

stable, solutions having concentrations between 2 and 5 mg/mL m -cresol are unstable, where the average micelle size changes within the 50 h experimental window. These unstable solutions are examined in the following section.

3.2. Growth Kinetics of Aggregating PS80/ m -Cresol Solutions. Solutions containing between 2 and 5 mg/mL m -cresol are unstable. Here, instability is defined as any solution

for which the scattering intensity curve (Figure 1) changes over the ≈ 50 h experimental window. In all solutions, instability results in increasing $R_g(t)$ (Figure 2) and $I_0(t)$ (Figure 3), which indicates aggregate formation and growth. m -Cresol concentrations that produce aggregating solutions are identified by the shaded region in Figure 5. In this instability regime, R_g (Figure 5a) and I_0 (Figure 5b) increase over time, resulting in ratios of $R_g(50)/R_{g,i}$ (Figure 5c) and $I_0(50)/I_{0,i}$ (Figure 5d) well above unity.

As was observed for the stable PS80/ m -cresol solutions, the aggregate density (I_0/R_g^3) remains nearly constant over time for most aggregating solutions (Figure 4). Solutions containing 2 and 4.5 mg/mL m -cresol are the only exceptions having aggregate densities that change with time. This phenomenon will be more closely examined in Section 4. Interestingly, the scattering invariant, Q^* , remains constant for all solutions, stable and unstable (Figure S2). Thus, in all cases, the total volume fraction of aggregates remains constant throughout the observation time frame.

Previous work observed that time-dependent R_g and I_0 measurements for a solution at different temperatures collapse onto a single master curve using time–temperature superposition.¹⁷ By applying this principle to solutions with varying m -cresol concentration, a similar master curve was found for R_g (Figure 2c) and I_0 (Figure 3c), where the data was collected at 22 °C. Data for each solution concentration was shifted onto the 3.15 mg/mL m -cresol data. The concentration-dependent shift factors, a and a_T , calculated using eq 10 are reported in

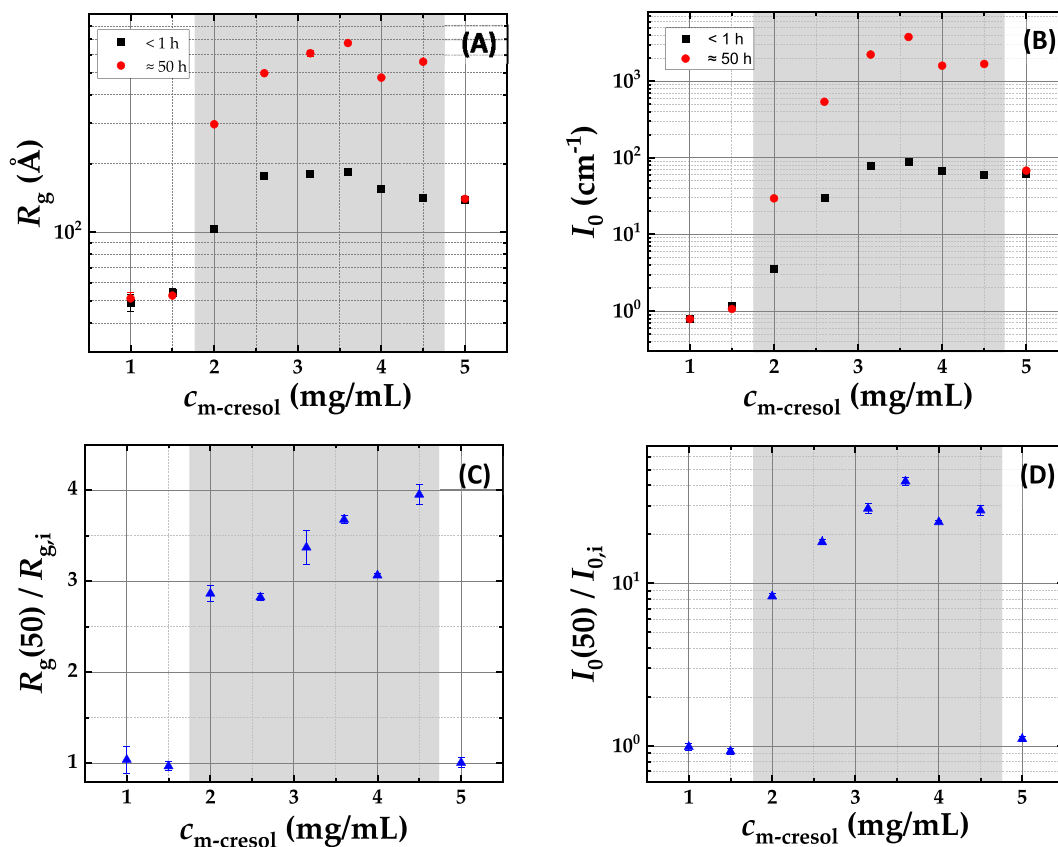


Figure 5. Phase diagram for (A) R_g (Å) and (B) I_0 (cm^{-1}) vs $c_{m-cresol}$ (mg/mL) comparing aggregate size and mass at short (<1 h, red ●) and long (≈ 50 h, ■) times, where the gray shading identifies the instability regime for PS80/ m -cresol aggregation. Ratios of final (after ≈ 50 h) and initial aggregate size (C) $R_g(50)/R_{g,i}$ and aggregate mass (D) $I_0(50)/I_{0,i}$, showing time invariance, or stability, at low and high m -cresol concentrations. The error bars represent 1 standard deviation and are often smaller than the plot symbols.

column 8 of Tables S5 and S6 along with the model fits. Collapse of time-shifted data onto a single master power-law slope of ≈ 0.4 supports the existence of a single governing coalescence mechanism for unstable PS80/*m*-cresol solutions at long times ($t/a \gtrsim 20$ h). However, there are differences in aggregation kinetics at short times for specific *m*-cresol concentrations (e.g., 4.5 mg/mL). Thus, regardless of the *m*-cresol concentration, early ($t/a \lesssim 20$ h) aggregation mechanisms lead to long-term coalescence and eventual phase separation of an oily droplet phase from the aqueous phase.

Aggregating PS80/*m*-cresol solutions can be subdivided into two types based on the growth mechanism. Type I solutions contain 2.0–3.6 mg/mL *m*-cresol and undergo a two-stage aggregation process. Type II solutions, having 4.0–4.5 mg/mL *m*-cresol, experience a three-stage aggregation mechanism. Figures 2a and 3a show examples of the different growth mechanisms for type I and type II aggregation.

The gray curve in Figure 2a (a 3.15 mg/mL *m*-cresol solution) is an example of two-stage type I aggregation, where a slow initial (incubation) stage (< 1 h) is followed by a power-law growth stage at long times. The power-law fit curve [eq 8] in Figure 2a helps illustrate the deviation of type I aggregation data from power-law behavior at short times, during the slow initial growth stage. The blue R_g curve for a 4.5 mg/mL *m*-cresol solution in Figure 2a is an example of three-stage type II aggregation. An initial incubation period (< 10 h) is followed by an exponential growth period ($10 \text{ h} < t < 30 \text{ h}$), which eventually yields to a power-law growth stage at long times (> 30 h). The length of each stage depends on the *m*-cresol concentration and temperature.

Type II aggregation kinetics can be modeled using eq 11, where the model fit is plotted in Figure 2a along with the data. Fit parameters are reported in Table S5. Type I aggregation kinetics can also be modeled with eq 11 when the barrier to micelle coalescence is negligible ($k_1 \rightarrow k_d$). A similar pattern arises for I_0 in Figure 3a, where the type I and type II aggregation kinetics can be modeled by eq 12. Equations 11 and 12 can describe both type I and type II aggregation kinetics, indicating that these seemingly different aggregation behaviors could result from the same kinetic mechanism. However, the type I and type II designations are maintained throughout this work to ease discussion. Solutions are classified as type I or type II using k_1 , where $k_1 \rightarrow k_d$ for type I and $0 < k_1 < k_d$ for type II. Only solutions containing 4 mg/mL or 4.5 mg/mL *m*-cresol experience type II aggregation based on these criteria. Solutions of 3.6 mg/mL *m*-cresol seem to be near the boundary between type I and type II. These solutions are included with type II aggregation analysis because they share the same initial spherical micelle morphology.

Both type I and type II solutions form aggregates from micelles having a morphology similar to one of the two stable micelle regimes discussed in Section 3.1. Type I aggregation begins from micelles most closely resembling the oblate ellipsoids/cylinders at low *m*-cresol concentrations (≤ 1.5 mg/mL *m*-cresol), and type II aggregation begins from micelles that are nearly spherical, similar to the microemulsion droplets in 5 mg/mL *m*-cresol solutions. This difference in initial morphology is illustrated by the open symbol plots in Figure 1b,c. The intensity curves at short times in Figure 1b have the same characteristic ellipsoidal micelle features at $q > 0.02 \text{ \AA}^{-1}$ that are observed for low *m*-cresol concentrations in Figure 1a. Similarly, the short-time intensity curves in Figure 1b have

characteristic spherical micelle features over the measured q range that agrees with the 5.0 mg/mL *m*-cresol solution in Figure 1a. Incidentally, all aggregating solutions have initial micelle morphologies resembling stable micelles with the closest *m*-cresol concentration. Thus, the initial building blocks for aggregate growth provide a useful method for classification aggregating PS80/*m*-cresol solutions.

3.3.1. Type I Aggregation Kinetics. Solutions with type I aggregation (2–3.15 mg/mL *m*-cresol) have k_1 that approaches k_d and experience two stages of aggregate growth: an initial stage of slow growth and a second stage of power-law growth. This defining aggregation mechanism is observed in Figure 2b for R_g and Figure 3b for I_0 . The $R_g(t)$ curves for *m*-cresol concentrations between 2 and 3.15 mg/mL have a period of slow growth at short times ($\lesssim 3$ h), followed by power-law growth at long times. This behavior can also be observed using hydrodynamic radius estimates from dynamic light scattering (DLS), shown in Figure S3. However, DLS is less reliable than SANS for turbid solutions, where multiple scattering becomes a concern. The growth kinetics for R_g (Figure 2b) and I_0 (Figure 3b) are modeled using of eqs 11 and 12, where fit parameters are reported in Tables S5 and S6. The zero-time I_0 , or $I_0(0)$, increases with the *m*-cresol concentration, which is echoed by $R_g(0)$. This suggests that the initial micelle/aggregate size increases with the *m*-cresol concentration. However, this difference in $R_g(0)$ or $I_0(0)$ causes challenges when generating the master curves of Figures 2c and 3c, where the data at short times ($t/a \lesssim 1$ h) does not converge to a single $R_g(0)$ or $I_0(0)$.

Model fitting of the scattering curves in Figure 1b reveals that the initial (< 1 h) micelle morphology for a 2.0 mg/mL *m*-cresol solution is cylindrical (Table S4), where the micelles are much larger than those of the stable solutions at lower *m*-cresol concentrations. The cylindrical micelle scattering features appear to be present at high- q ($q > 0.02 \text{ \AA}^{-1}$) in the other initial scattering curves of Figure 1b. This suggests that these solutions may all begin aggregating from cylindrical micelles. Whereas high- q scattering is dominated by small cylindrical micelles, low- q scattering at $q \leq 0.02 \text{ \AA}^{-1}$ corresponds to aggregate morphology. In Figure 1b, the core-shell ellipsoid model fits of low- q scattering at short times (< 1 h) show that aggregates form rapidly. Solutions containing 3.15 mg/mL *m*-cresol aggregate fastest, resulting in the largest initial aggregate size. Aggregate model fits for 2.6 and 3.15 mg/mL *m*-cresol solutions are shown for $q \leq 0.02 \text{ \AA}^{-1}$. These model fits disagree with scattering data at high q , where scattering intensity does not reflect the aggregate size. Thus, model fits for 2.6 and 3.15 mg/mL *m*-cresol are curtailed at $q = 0.03 \text{ \AA}^{-1}$. Table S4 details the fit parameters.

3.3.2. Type II Aggregation Kinetics. Type II aggregation has three stages: an initial slow growth/incubation stage, an exponential growth stage, and a power-law growth stage at long times. The duration of each stage is dependent on *m*-cresol concentration and temperature, where $0 < k_1 < k_d$. From kinetic R_g (Figure 2b) and I_0 (Figure 3b) data, solutions with 4.0–4.5 mg/mL *m*-cresol experience these three aggregation stages within the ≈ 50 h observation period. Applying eqs 11 and 12, the model fits for these solutions are reported in Tables S5 and S6. The fitted $R_g(0)$ or $I_0(0)$ values approach that of the stable formulation condition at 5 mg/mL *m*-cresol. A good fit for this parameter is difficult to achieve for the 3.6 mg/mL *m*-cresol solution because the growth kinetics in this solution are too fast. The 3.6 mg/mL *m*-cresol formulation has

the fastest growth kinetics of any solution tested and represents the maximum aggregation speed for PS80/*m*-cresol solutions.

The sometimes long incubation times for type II solutions (e.g., 4.5 mg/mL *m*-cresol) also presents a challenge for generating an accurate time-shifted master curve for R_g (Figure 2c) and I_0 (Figure 3c). However, the power-law growth regimes at long times agree. This provides evidence that a single mechanism governs long-term aggregate coalescence, while the onset of this coalescence is determined by *m*-cresol concentrations via incubation time.

Figure 1c demonstrates that the initial scattering curves for these type II aggregating solutions are similar, where an ellipsoid core-shell model (Table S4) fits well. The fitted initial micelle morphology is nearly spherical and approaches the size and shape of stable microemulsion droplets in the 5 mg/mL *m*-cresol solution. This similarity to stable solution morphologies provides insight into the source of the ≈ 10 h incubation period observed for 4.5 mg/mL *m*-cresol solutions. This also suggests that type II aggregation begins from nearly spherical micelles/aggregates, whereas type I aggregation is likely initiated from cylindrical aggregates as discussed in the previous section.

3.4. Effect of PS80 Concentration on Solution Aggregation. The aggregation behavior was studied in solutions containing 0.2 and 1.0 mg/mL PS80 with varying *m*-cresol concentrations. Figure 6 shows that solutions having a

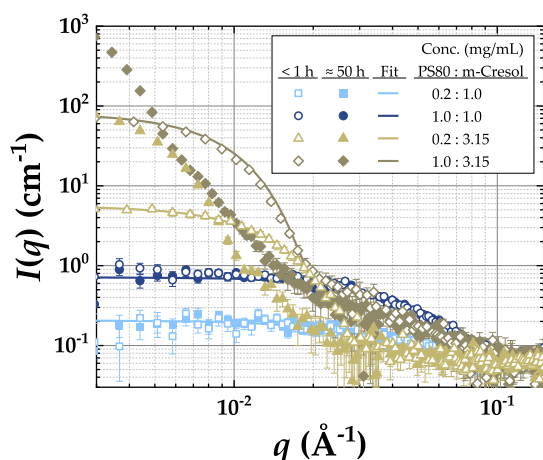


Figure 6. $I(q)$ (cm^{-1}) vs q (\AA^{-1}) plots of unbuffered 0.2 and 1.0 mg/mL PS80 solutions with 1.0 and 3.15 mg/mL *m*-cresol in D_2O at $T = 22$ °C with core-shell ellipsoid model fits for growth times of <1 h ($\square, \circ, \triangle, \diamond$) and ≈ 50 h ($\blacksquare, \bullet, \blacktriangle, \blacklozenge$), where fit parameters are detailed in Tables S3 and S4 of the Supporting Information. The error bars represent 1 standard deviation and are often smaller than the plot symbols.

lower PS80 content (0.2 mg/mL) experience aggregation similar to solutions having 1.0 mg/mL PS80. The reduced scattering intensity for 0.2 mg/mL PS80 solutions is expected as scattering intensity scales with volume fraction. The initial (<1 h) and final (≈ 50 h) scattering curves in Figure 6 are nearly identical for solutions containing 1 mg/mL *m*-cresol, regardless of the PS80 concentration. This indicates that these solutions are kinetically stable and do not aggregate over the experimental time frame. As with the 1 mg/mL PS80 solutions discussed previously, solutions containing 3.15 mg/mL *m*-cresol and 0.2 mg/mL PS80 aggregate. However, based on the R_g and I_0 calculated from the final (≈ 50 h) scattering curves in

Figure 6, the size of aggregates is smaller in solutions containing 0.2 mg/mL PS80 than in those having 1.0 mg/mL PS80. Thus, the PS80 concentration influences the aggregate size without altering the solution stability.

The time-dependence of R_g (Figure 7a) and I_0 (Figure 8a) for 0.2 mg/mL PS80 solutions follows the same kinetic models

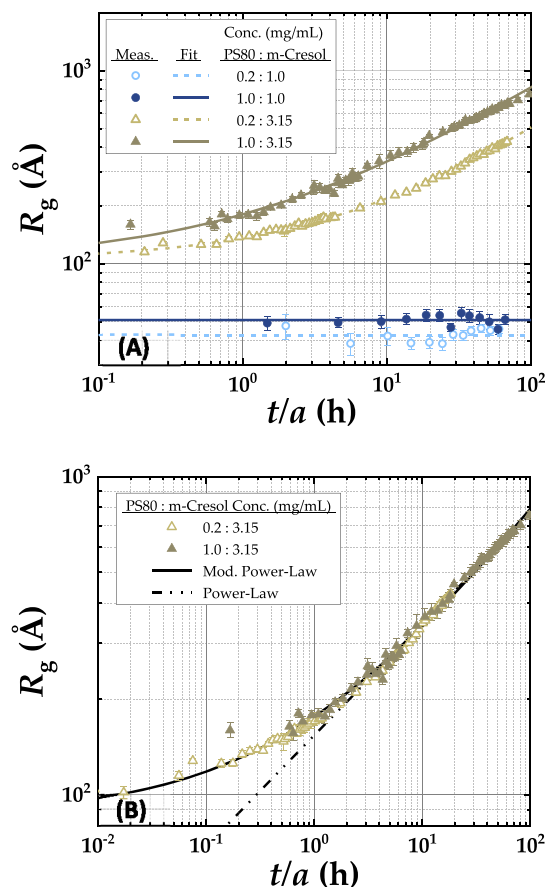


Figure 7. R_g (\AA) vs t_a (h) (A) plot of unbuffered 0.2 mg/mL (\circ, \triangle) and 1.0 mg/mL PS80 (\bullet, \blacktriangle) solutions with 1 and 3.15 mg/mL *m*-cresol in D_2O at $T = 22$ °C with kinetic model fits [eq 11], where fit parameters are detailed in Table S5 of the Supporting Information, and (B) time-shifted master curve of 0.2 mg/mL PS80 with 3.15 mg/mL *m*-cresol ($a = 3.72$) and 1.0 mg/mL PS80 with 3.15 mg/mL *m*-cresol ($a = 1.0$) along with kinetic model fits ($k_1 \rightarrow k_4$), $R_g = 89.9 \cdot (t/a)^{0.448} + 86.3$ (\AA), and power-law fit, $R_g = 154 \cdot (t/a)^{0.349}$ (\AA). The error bars represent 1 standard deviation.

as their 1 mg/mL PS80 analogues. However, the parameter fits differ to account for the smaller aggregate sizes present in 0.2 mg/mL PS80 solutions. The kinetic model fit parameters for R_g and I_0 are reported in Tables S5 and S6. At both PS80 concentrations, 3.15 mg/mL *m*-cresol solutions aggregation kinetics can be described using eqs 11 and 12. This suggests that only the aggregate size is dependent on the PS80 concentration, while the mechanism of aggregation is independent of the PS80 concentration.

R_g and I_0 data at different PS80 concentrations can be collapsed onto a single master curve by shifting the power-law region of the 0.2 mg/mL PS80 solution onto that of the 1.0 mg/mL PS80 solution (Figures 7b and 8b). The PS80 concentration-dependent shift factors are reported in Tables S5 and S6. The time shifts in Figures 7 and 8 reveal that $R_g(0)$ and $I_0(0)$ are larger for 1 mg/mL PS80 solutions than for 0.2

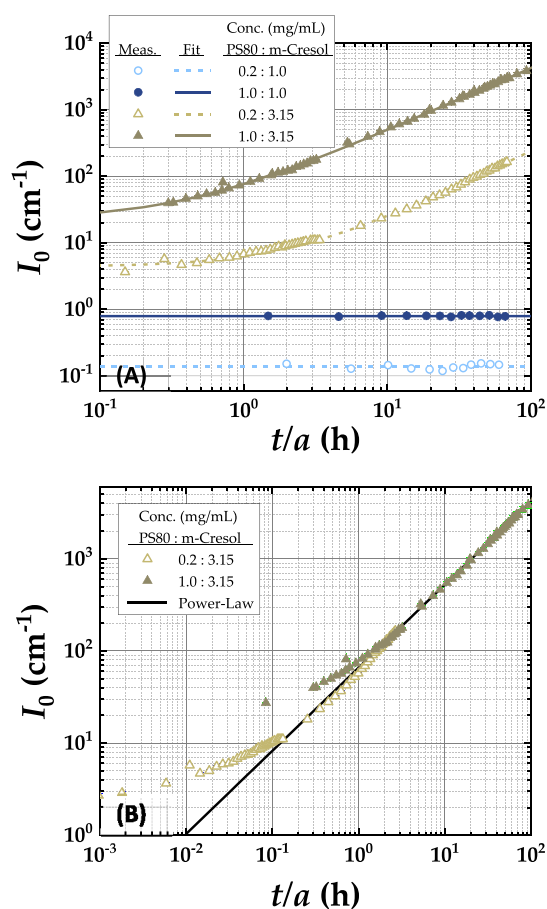


Figure 8. I_0 (cm^{-1}) vs t/a (h) (A) plot of unbuffered 0.2 mg/mL (\circ , \triangle) and 1.0 mg/mL (\bullet , \blacktriangle) PS80 solutions with 1 and 3.15 mg/mL *m*-cresol in D_2O at $T = 22$ °C with kinetic model fits [eq 12], where model fits are reported in Table S6, and (B) time-shifted master curve of 0.2 mg/mL PS80 and 3.15 mg/mL *m*-cresol ($a = 3.72$) and 1.0 mg/mL PS80 and 3.15 mg/mL *m*-cresol ($a = 1.0$) along with power-law model fit, $I_0 = 65.7 \cdot (t/a)^{0.902}$ (cm^{-1}), for $2.0 \text{ h} \leq t/a_T \leq 100 \text{ h}$. The error bars represent 1 standard deviation.

mg/mL PS80 solutions. This agrees with the trend observed in the *m*-cresol concentration series discussed above, where increased *m*-cresol content results in larger $R_g(0)$ and $I_0(0)$. The difference in $R_g(0)$ and $I_0(0)$ between 0.2 and 1.0 mg/mL PS80 solutions makes it impossible to shift short time (<1 h) data accurately. Thus, the master curve only provides insight into the shared power-law aggregate growth region.

4. DISCUSSION

The phase diagram of PS80/*m*-cresol solution aggregation in Figure 5 reveals how the *m*-cresol concentration directs the aggregate morphology and stability. The gray-shaded region of Figure 5 between ≈ 2.0 and ≈ 4.5 mg/mL *m*-cresol corresponds to an instability regime, where micelles form aggregates that grow or coalesce over time. Aggregation in this instability regime progresses through a multi-stage mechanism, as shown in Figures 2b and 3b. All aggregating solutions experience an initial stage of incubation or slow growth and a final stage of aggregate coalescence. The coalescence of aggregates has a power-law dependence on time at sufficiently long times ($t/a \gtrsim 10$ h in Figure 2c), and aggregate growth continues until oily PS80/*m*-cresol droplets phase-separate from the aqueous D_2O phase. At room temperature, total phase separation can occur

after approximately 2 months to a year depending on the *m*-cresol concentration, where solutions containing 3.6 mg/mL *m*-cresol achieve phase separation fastest. More observation is necessary to characterize these ultra-long-term kinetics. The phase diagram in Figure 5 also correlates with solution turbidity (Figure S4), where stable solutions are transparent and unstable solutions become cloudy.

Figure 5 also identifies two regimes of PS80/*m*-cresol solution stability that bookend the instability regime. Stability is represented here by time-invariant R_g (Figure 5a) and I_0 (Figure 5b) and by $R_g(50)/R_{g,i}$ (Figure 5c) and $I_0(50)/I_{0,i}$ (Figure 5d) ratios near unity. These stability regimes at *m*-cresol concentrations below 2 mg/mL and above 4.5 mg/mL present possible conditions that practitioners may use to produce stable formulations. Solutions classified as “stable” in this study are only kinetically stable, where no aggregation occurs over the ≈ 50 h measurement period. Times after 50 h are beyond the scope of this work, but it is speculated that some “stable” solutions may aggregate after 50 h. It is also well understood that PS80 is capable of degradation after approximately 28 days.⁶ This places an additional time constraint on PS80/*m*-cresol solution stability.

From the model fits of stable solutions in Figure 1a, the PS80 molecules self-assemble into core–shell prolate ellipsoids or short cylinders. The shell contains the hydrophilic PS80 headgroups, and the core protects the hydrophobic tails. The preferred stable micelle morphology (ellipsoid or cylinder) depends on the *m*-cresol concentration. This suggests that *m*-cresol is incorporated into the micelles in different amounts based on the amount of *m*-cresol available in solution. This *m*-cresol-induced micelle swelling causes a transition from prolate ellipsoidal micelles in PS80 solutions containing 0 and 1.0 mg/mL *m*-cresol to cylindrical micelles in solutions with 1.5 mg/mL *m*-cresol. Thus, micelles elongate to accommodate more *m*-cresol at low concentrations. Above 1.5 mg/mL *m*-cresol, micelles can no longer pack *m*-cresol in a way that preserves micelle stability, causing swelling and coalescence. The underlying mechanism connecting micelle packing with PS80/*m*-cresol intermolecular interactions is still unclear.

At 5 mg/mL *m*-cresol, a microemulsion is formed with droplets having an R_g approximately 3 times larger than the micelles formed in the stability regime at low *m*-cresol concentrations (<2.0 mg/mL). These microemulsion droplets are nearly spherical ellipsoids, where the core likely consists mostly of *m*-cresol. Although further study is needed to more accurately determine where *m*-cresol resides within the micelles, the present work reveals two micelle morphologies that are available for stabilizing PS80/*m*-cresol solutions. Figure S1 summarizes stable PS80/*m*-cresol micelle morphologies with approximate illustrations. This finding also translates to PS80/*m*-cresol solutions containing only 0.2 mg/mL PS80 (Figures 6–8). In these lower PS80 concentration solutions, stable ellipsoidal micelles are also formed in the presence of 1 mg/mL *m*-cresol. This suggests that PS80/*m*-cresol solution stability is primarily influenced by *m*-cresol content. However, the PS80 concentration contributes to micelle size, where reduced PS80 concentration corresponds to smaller micelles.

The scattering patterns for oblate and prolate ellipsoidal micelles are nearly indistinguishable at the observed small aspect ratios. Previous modeling efforts characterized the ellipsoidal PS80 micelles as oblate,^{7,17} as there was no evidence to favor prolate over oblate morphologies. Here, a transition from ellipsoidal to cylindrical micelles was observed with

increasing *m*-cresol concentrations. Thus, we postulate that the ellipsoidal micelles are prolate rather than oblate to accommodate the elongation necessary for this morphological transition, as elongation would occur along the polar ellipsoidal axis. Thus, it is more likely that the polar axis is the major ellipsoidal axis, making the micelles prolate. The formation of prolate ellipsoids in solutions containing only 1 mg/mL PS80 is also consistent with the findings of Aizawa (2009).¹⁹

The stability regimes of Figure 5 correspond to acceptable conditions for stable micelle formation. However, the *m*-cresol concentrations within the gray-shaded region of Figure 5 produce unstable solutions that aggregate with time. This indicates that no stable micelle or aggregate morphology can be achieved at these concentrations. In the present discussion, our attention is focused on the growth kinetics in these aggregating solutions.

The proposed mechanistic equation [eq 11] captures the evolution of aggregate R_g with time for PS80/*m*-cresol solutions containing between 0 and 5 mg/mL *m*-cresol. The kinetic equation is also adapted to I_0 measurements in eq 12. As is detailed above in Section 2.5, there are three parts to the proposed mechanism: $R_g(0)$ describing the initial micelle size, the power-law term characterizing coalescence at long times, and the exponential reaction term that introduces rate constants for aggregate formation (k_1 , k_2). Two aggregation types were identified in Section 3.2, where type II aggregation has a finite energy barrier to aggregate coalescence ($0 < k_1 < k_d$) that is not present in type I aggregation ($k_1 \rightarrow k_d$). Figures 2a and 3a provide examples of type I and type II aggregation. Stable solutions are a special case of eq 11, where the barrier to aggregate coalescence is insurmountable ($k_1 \rightarrow 0$). Thus, eqs 11 and 12 can describe the stability and instability observed in each of the PS80/*m*-cresol solutions examined. The kinetic model fits of R_g and I_0 are presented in Figures 2, 3, 7, and 8, where the fitted model parameters are reported in Tables S5 and S6 of the Supporting Information.

The kinetic model fits in Figures 2b and 7b reveal a general increase in initial R_g or $R_g(0)$, with *m*-cresol and PS80 concentrations from 30 Å in 1 mg/mL PS80 only solutions to 146 Å in 1 mg/mL PS80 solutions containing 4.5 mg/mL *m*-cresol. This suggests that micelles in both stable and unstable PS80/*m*-cresol solutions attempt to incorporate *m*-cresol proportional to the total *m*-cresol concentration. Additionally, the increase in $R_g(0)$ with the PS80 concentration indicates that the micelle size is also limited by the amount of available PS80. However, previous work showed that changes in PS80 concentration in solutions without *m*-cresol did not alter the radius of gyration.¹⁷ Thus, it is likely the interaction between *m*-cresol and PS80 that causes the aggregate size to depend on the PS80 concentration.

The $I_0(0)$ model fits also become larger with increased *m*-cresol concentrations, and this trend is more consistent than in the case of $R_g(0)$. The $I_0(0)$ model fits are reported in Table S6 and visualized in Figures 7b and 8b. $I_0(0)$ increases monotonically from 0.106 cm⁻¹ for micelles formed in 0.2 mg/mL PS80 solutions without *m*-cresol to 67.1 cm⁻¹ in solutions of 1 mg/mL PS80 with 5 mg/mL *m*-cresol. This increase in initial aggregate mass, represented by $I_0(0)$, with the component concentration suggests that the micelles incorporate material proportional to the total solution concentration. Higher concentrations of either PS80 or *m*-cresol will increase the initial aggregate size. This would suggest that the composition of these initial aggregates is also

dependent on the concentration of each component, which impacts the morphology and packing.

The master curve plots in Figures 2c and 8c of data shifted based on *m*-cresol and PS80 concentrations show that the short-time $R_g(0)$ and $I_0(0)$ do not collapse onto a single curve, as expected. The modified power-law fit in Figures 2c and 7c approaches an average $R_g(0)$ that is not characteristic of all PS80/*m*-cresol solutions. However, the power-law fits in Figures 2, 3, 7, and 8 provide a useful characteristic slope estimate of ≈ 0.4 for R_g and ≈ 1 for I_0 . Thus, whereas power-law coalescence at long times is not dependent on the initial aggregate size, the path and time to get to the power-law growth stage is influenced by the initial aggregate size. In other words, the stability of the starting conditions, $R_g(0)$ and $I_0(0)$, influence the mechanism of aggregation: type I, type II, or no aggregation. For example, the conditions in a 1 mg/mL PS80 solution with 4.5 mg/mL *m*-cresol provide enough stability to allow for a 10 h incubation time, where the solution is seemingly stable. However, eventually, the micelles in solution can no longer maintain a stable morphology at long times. This strange behavior of type II aggregating samples is characterized by a finite barrier to coalescence, $0 < k_1 < k_d$.

Micelle coalescence is prevented in stable solutions by an insurmountable energy barrier ($k_1 = 0$), where stable micelles prefer to repel each other rather than coalesce. Thus, in unstable solutions, this barrier is either low or nonexistent, indicating that the micelles are unable to organize themselves into a sufficiently stable morphology to prevent coalescence. For solutions containing between 2 and 3.15 mg/mL *m*-cresol (type I), the barrier to coalescence is negligible ($k_1 \rightarrow k_d$), and the solutions enter power-law coalescence immediately following a slow growth stage (Figure 2), where micelles swell and attempt to achieve a stable morphology. SANS measurements at short times (<1 h) reveal aggregate structures that have some cylindrical features that are characteristic of stable 1.5 mg/mL *m*-cresol solutions supporting this hypothesis for early growth. However, data for solutions at shorter timescales are necessary to confirm short-time behavior. Unfortunately, our neutron scattering results do not have sufficient time resolution to assess times under 10 min.

In solutions with 4.0–4.5 mg/mL *m*-cresol (type II), k_1 is finite and nonzero. This causes the solution to experience a third stage of exponential (sigmoidal) aggregation between the early stage and the power-law stage. The 4.5 mg/mL *m*-cresol solution provides the most obvious example of this phenomenon. The metastability of the initial micelles is a result of a small but nonzero k_1 such that it takes 10 h before aggregation begins. The length of this metastable stage is influenced by k_2 , which controls the autocatalytic reaction step. Metastability is likely a result of a nearly stable initial micelle morphology similar to that of the kinetically stable 5 mg/mL *m*-cresol solutions. Though its effects are observed and kinetically modeled here, the underlying molecular mechanism causing the disruption of this metastable stage is unknown. Once the energy barrier to aggregation is surpassed and micelles begin to coalesce, exponential reaction-limited coalescence continues until all the aggregates are formed. At this point, aggregation continues through diffusion-limited power-law coalescence.

Section 3.2 introduced the observation that the aggregate density, I_0/R_g^3 , increases with the *m*-cresol concentration for aggregating solutions (Figure 4). To accommodate higher *m*-

cresol concentrations, more *m*-cresol must be included in the aggregates. This results in denser aggregates likely containing mostly *m*-cresol, as suggested by the estimated volume fraction (Table S4). I_0/R_g^3 is nearly time invariant for all solutions, except for solutions containing 2 and 4.5 mg/mL *m*-cresol. This supports the observation that most aggregating solutions form nearly spherical aggregates that grow radially with time. Because I_0/R_g^3 changes with time for the 2 and 4.5 mg/mL *m*-cresol solutions, the aggregates in these solutions are less spherical and grow along one axis more than others. This is likely a result of these solutions having concentrations close to the lower and upper stability boundaries in Figure 5. Thus, a metastability may exist in these solutions which likely contributes to their outlier behavior. Additionally, the scattering invariant (Figure S2) for these solutions does not change with time. This indicates that the change in aggregate density is not caused by a change in total aggregate volume fraction.

At 2 mg/mL *m*-cresol, the aggregate density decreases gradually with time. Figures 1b–3b show that this solution aggregates the slowest and has the smallest aggregate size, where the R_g and I_0 power-law slopes of ≈ 0.33 and ≈ 0.53 for the 2 mg/mL *m*-cresol solution are lower than ≈ 0.4 and ≈ 1 for other aggregating solutions. Paired with the decrease in time-dependent I_0/R_g^3 , the smaller power-law slope signals the formation of aggregates with a larger aspect ratio, where they are less spherical than the aggregates formed in other solutions. The 2 mg/mL *m*-cresol solution has a constant I_0/R_g^2 ratio further supporting the hypothesis that aggregates grow through the widening of cylinder cross-sectional area rather than in all directions.

PS80 solutions with 4.5 mg/mL *m*-cresol experience a temporary decrease in I_0/R_g^3 during the sigmoidal exponential growth stage (≈ 17 h). Once aggregate growth approaches the power-law stage, the density begins to rebound. The density may fully recover to that of the induction stage, but a longer measurement time is needed to confirm this. None of the other type II aggregating solutions experience this stage of changing I_0/R_g^3 despite having sigmoidal growth stages. This unique feature of 4.5 mg/mL *m*-cresol solutions may be a result of a nonzero k_2 , which corresponds to a steeper sigmoid slope. During the exponential growth stage, aggregate R_g doubles and I_0 increases by 30-fold. This massive reorganization of aggregates is the cause of I_0/R_g^3 time dependence. The increase in aggregate mass, I_0 , lags the swelling of the aggregate volume, R_g^3 . This explains the initial drop in and gradual recovery of the density.

Because the scattering invariant is constant throughout all measurements, the morphological reorganization that occurs during the sigmoidal growth stage occurs entirely between the existing micelles/aggregates. No additional material is incorporated as the volume and mass increase in each aggregate. Once the sigmoidal stage completes, PS80 solutions with 4.5 mg/mL *m*-cresol enter the final stage of power-law coalescence that other solutions experience.

5. CONCLUSIONS

A stability-phase diagram for PS80/*m*-cresol solutions (Figure 5) summarizes our findings and is a main result of this work. PS80/*m*-cresol solutions are stable for *m*-cresol concentrations $\lesssim 1.5$ and $\gtrsim 5$ mg/mL, where no aggregate growth is observed during the 50 h experimental window. Solutions containing *m*-cresol concentrations between the upper and lower stability

regimes ($1.5 \text{ mg/mL} \lesssim c_{m\text{-cresol}} \lesssim 5 \text{ mg/mL}$) are unstable, having aggregates that increase in size over time. These stability and instability regimes are not influenced by the PS80 concentration. Our results indicate that solution stability is determined by the *m*-cresol concentration.

Stable PS80/*m*-cresol solutions form cylindrical or prolate ellipsoidal micelles. In the upper stability regime ($c_{m\text{-cresol}} \gtrsim 5 \text{ mg/mL}$), stable micelles incorporate large amounts of *m*-cresol and form a stable microemulsion of nearly spherical droplets. Micelles in the lower stability regime ($c_{m\text{-cresol}} \lesssim 1.5 \text{ mg/mL}$) are 27 times smaller than the droplets in the upper regime and are generally less spherical. This suggests a limited set of micelle morphologies suitable for generating stable PS80/*m*-cresol solutions, where the *m*-cresol concentration determines if any of these micelle morphologies can be achieved. When the *m*-cresol concentration falls within the instability regime ($1.5 \text{ mg/mL} \lesssim c_{m\text{-cresol}} \lesssim 5 \text{ mg/mL}$), no stable micelle morphology or molecular packing can be achieved, and the micelles begin to swell and coalesce. These insights into PS80/*m*-cresol aggregate morphology are a main result of this work.

A single kinetic model can describe each stage of aggregation [eqs 11 and 12]. Equations 11 and 12 are a main result of this work and reveal that solution stability is characterized by aggregation rate constants, k_1 and k_2 , where stable micelles have an insurmountable repulsion force ($k_1 \rightarrow 0$) that prevents aggregation. The model also shows coalescence is diffusion limited and proceeds immediately after nucleation in solutions with a negligible barrier to coalescence ($k_1 \rightarrow k_d$). This coalescence eventually results in phase separation of oily PS80/*m*-cresol droplets from the aqueous phase. k_1 and k_2 vary with the *m*-cresol concentration, suggesting that *m*-cresol may modify the repulsive forces between micelles as well as micelle morphology. Overall, the aggregation rate increases with the *m*-cresol concentration up to a maximum at ≈ 3.6 mg/mL *m*-cresol, above which the aggregate growth slows.

While our results advance the understanding of PS80/*m*-cresol incompatibility and define clear boundaries to formulation stability via a stability phase diagram, there is still little understanding of how *m*-cresol associates with PS80 to cause changes in morphology and stability. Combining SANS contrast matching with complementary scattering techniques may reveal this information. This would also verify the micelle morphology proposed in this study. The presented kinetic model [eqs 11 and 12] provides a framework for describing the evolution of aggregates with time. However, to fully understand PS80/*m*-cresol stability, a more predictive model must be developed by determining how the preservative concentration influences k_1 and k_2 . This would accelerate formulation science by allowing for a priori determination of formulation stability.

■ ASSOCIATED CONTENT

SI Supporting Information

The Supporting Information is available free of charge at <https://pubs.acs.org/doi/10.1021/acs.molpharmaceut.1c00803>.

Kinetic model derivation, complimentary measurements of aggregate size (DLS and scattering invariant), and images of aggregating samples (PDF)

AUTHOR INFORMATION

Corresponding Authors

Ken K. Qian – Eli Lilly and Company, Indianapolis, Indiana 46225, United States; Email: qian_ken_k@lilly.com

Norman J. Wagner – Department of Chemical and Biomolecular Engineering Department, Center for Neutron Science, University of Delaware, Newark, Delaware 19716, United States; orcid.org/0000-0001-9565-619X; Email: wagnernj@udel.edu

Yun Liu – Department of Chemical and Biomolecular Engineering Department, Center for Neutron Science, University of Delaware, Newark, Delaware 19716, United States; NIST Center for Neutron Research, National Institute of Standards and Technology, Gaithersburg, Maryland 20899, United States; orcid.org/0000-0002-0944-3153; Email: yun.liu@nist.gov

Authors

Peter H. Gilbert – Department of Chemical and Biomolecular Engineering Department, Center for Neutron Science, University of Delaware, Newark, Delaware 19716, United States; NIST Center for Neutron Research, National Institute of Standards and Technology, Gaithersburg, Maryland 20899, United States; orcid.org/0000-0003-1707-7517

Zhenhuan Zhang – Department of Chemical and Biomolecular Engineering Department, Center for Neutron Science, University of Delaware, Newark, Delaware 19716, United States; NIST Center for Neutron Research, National Institute of Standards and Technology, Gaithersburg, Maryland 20899, United States; orcid.org/0000-0001-5684-7268

David P. Allen – Eli Lilly and Company, Indianapolis, Indiana 46225, United States

Rachel Ford – Department of Chemical and Biomolecular Engineering Department, Center for Neutron Science, University of Delaware, Newark, Delaware 19716, United States; NIST Center for Neutron Research, National Institute of Standards and Technology, Gaithersburg, Maryland 20899, United States

Complete contact information is available at:

<https://pubs.acs.org/10.1021/acs.molpharmaceut.1c00803>

Notes

The authors declare no competing financial interest.

ACKNOWLEDGMENTS

Certain commercial equipment, instruments, or materials (or suppliers, or software, etc.) are identified in this paper to foster understanding. Such identification does not imply recommendations or endorsements by the National Institute of Standards and Technology, nor does it imply that the materials or equipment identified are necessarily the best available for the purpose. We are grateful to the members of NCNR for their help during data collection and analysis. Access to vSANS was provided by the Center for High Resolution Neutron Scattering, a partnership between the National Institute of Standards and Technology and the National Science Foundation under agreement no. DMR-1508249. This work benefited from the use of the SasView application, originally developed under NSF Award DMR-0520547. SasView also contains a code developed with funding from the EU Horizon 2020 programme under the SINE2020 project grant no.

654000. This research was performed while the author held an NRC Research Associateship award at the NCNR.

REFERENCES

- (1) Janssen Biotech, Inc. *Remicade: Highlights of Prescribing Information*: Horsham, PA, 2017.
- (2) Eli Lilly and Company. *Trulicity: Highlights of Prescribing Information*: Indianapolis, IN, 2020.
- (3) Regeneron Pharmaceuticals, Inc. *Eylea: Highlights of Prescribing Information*: Tarrytown, NY, 2019.
- (4) Weiss, W. F.; Young, T. M.; Roberts, C. J. Principles, approaches, and challenges for predicting protein aggregation rates and shelf life. *J. Pharm. Sci.* **2009**, *98*, 1246–1277.
- (5) Lowe, D.; Dudgeon, K.; Rouet, R.; et al. Aggregation, stability, and formulation of human antibody therapeutics. *Adv. Protein Chem. Struct. Biol.* **2011**, *84*, 41–61.
- (6) Shi, S.; Chen, Z.; Rizzo, J. M.; et al. A highly sensitive method for the quantitation of polysorbate 20 and 80 to study the compatibility between polysorbates and m-cresol in the peptide formulation. *J. Anal. Bioanal. Tech.* **2015**, *6*, 2.
- (7) Nayem, J.; Zhang, Z.; Tomlinson, A.; et al. Micellar morphology of polysorbate 20 and 80 and their ester fractions in solution via small-angle neutron scattering. *J. Pharm. Sci.* **2020**, *109*, 1498–1508.
- (8) Tomlinson, A.; Demeule, B.; Lin, B.; Yadav, S. Polysorbate 20 degradation in biopharmaceutical formulations: quantification of free fatty acids, characterization of particulates and insights into the degradation mechanism. *Mol. Pharm.* **2015**, *12*, 3805–3815.
- (9) Tomlinson, A.; Zarraga, I. E.; Demeule, B. Characterization of polysorbate ester fractions and implications in drug product stability. *Mol. Pharm.* **2020**, *17*, 2345–2353.
- (10) Dwivedi, M.; Blech, M.; Presser, I.; Garidel, P. Polysorbate degradation in biotherapeutic formulation: identification and discussion of current root causes. *Int. J. Pharm.* **2018**, *552*, 422–436.
- (11) Hewitt, D.; Alvarez, M.; Robinson, K.; et al. Mixed-mode and reversed-phase liquid chromatography-tandem mass spectrometry methodologies to study composition and base hydrolysis of polysorbate 20 and 80. *J. Chromatogr. A* **2011**, *1218*, 2138–2145.
- (12) Kerwin, B. A. Polysorbates 20 and 80 used in the formulation of protein biotherapeutics: structure and degradation pathways. *J. Pharm. Sci.* **2008**, *97*, 2924–2935.
- (13) Meyer, B. K.; Ni, A.; Hu, B.; Shi, L. Antimicrobial preservative use in parenteral products: Past and present. *J. Pharm. Sci.* **2007**, *96*, 3155–3167.
- (14) Galichet, L. Y. Cresol. In *Handbook of Pharmaceutical Excipients*, 6th ed.; Rowe, R. C., Sheskey, P. J., Quinn, M. E., Eds.; Pharmaceutical Press, London and American Pharmacists Association: Washington, 2009; pp 203–205.
- (15) Knoch, H.; Ulbrich, M. H.; Mittag, J. J.; et al. Complex micellization behavior of the polysorbates tween 20 and tween 80. *Mol. Pharm.* **2021**, *18*, 3147–3157.
- (16) Garidel, P.; Blech, M.; Buske, J.; Blume, A. Surface tension and self-association properties of aqueous polysorbate 20 HP and 80 HP solutions: Insights into protein stabilization mechanisms. *J. Pharmaceut. Innovat.* **2021**, *16*, 726.
- (17) Gilbert, P. H.; Zhang, Z.; Qian, K. K.; et al. Preservative Induced Polysorbate 80 Micelle Aggregation. *J. Pharm. Sci.* **2021**, *110*, 2395–2404.
- (18) Ludwig, M.; Geisler, R.; Prévost, S.; von Klitzing, R. Shape and structure formation of mixed nonionic-anionic surfactant micelles. *Molecules* **2021**, *26*, 4136.
- (19) Aizawa, H. Morphology of polysorbate 80 (Tween 80) micelles in aqueous 1,4-dioxane solutions. *J. Appl. Crystallogr.* **2009**, *42*, 592–596.
- (20) Aizawa, H. Morphology of polysorbate 80 (Tween 80) micelles in aqueous dimethyl sulfoxide solutions. *J. Appl. Crystallogr.* **2010**, *43*, 630–631.
- (21) Aizawa, H. Effect of increasing N,N-dimethylformamide concentration on the structure of polysorbate 80 micelles. *Open Chem. Phys. J.* **2011**, *3*, 6–9.

- (22) Bartling, C. M.; Andre, J. C.; Howland, C. A.; et al. Stability characterization of a polysorbate 80-dimethyl trisulfide formulation, a cyanide antidote candidate. *Drugs R* **2016**, *16*, 109–127.
- (23) Ashkar, R.; Bilheux, H. Z.; Bordallo, H.; et al. Neutron scattering in the biological sciences: progress and prospects. *Acta Crystallogr., Sect. D: Struct. Biol.* **2018**, *74*, 1129–1168.
- (24) Mohajeri, E.; Noudeh, G. D. Effect of temperature on the critical micelle concentration and micellization thermodynamic of nonionic surfactants: polyoxyethylene sorbitan fatty acid esters. *E-J. Chem.* **2012**, *9*, 2268–2274.
- (25) Carter, J. S.; Hardy, R. K. XVIII.-The salting-out effect. Influence of electrolytes on the solubility of m-cresol in water. *J. Chem. Soc.* **1928**, *0*, 127–129.
- (26) Kline, S. R. Reduction and analysis of SANS and USANS data using IGOR Pro. *J. Appl. Crystallogr.* **2006**, *39*, 895–900.
- (27) Doucet, M.; Cho, J. H.; Alina, G.; et al. *SasView*, Version 5.0.4, Zenodo, 2021, DOI: 10.5281/zenodo.4467703.
- (28) Sivia, D. S. *Elementary Scattering Theory*; Oxford University Press Inc.: New York, 2011; pp 63–92.
- (29) Porod, G. General Theory. In *Small-Angle X-ray Scattering*; Glatter, O., Kratky, O., Eds.; Academic Press Inc.: New York, 1982; pp 17–52.
- (30) Porod, G. Die Röntgenkleinwinkelstreuung von dichtgepackten kolloiden Systemen. *Kolloid-Z.* **1951**, *124*, 83–114.
- (31) NIST IGOR/DANSE. core_shell_ellipsoid. *SasView* 5.0.3 Documentation. March 27, 2019. http://www.sasview.org/docs/user/models/core_shell_ellipsoid.html (accessed Jan 19, 2022).
- (32) Hanus, L. H.; Hartzler, R. U.; Wagner, N. J. Electrolyte-induced aggregation of acrylic latex. 1. Dilute particle concentrations. *Langmuir* **2001**, *17*, 3136–3147.
- (33) Lin, M. Y.; Lindsay, H. M.; Weitz, D. A.; et al. Universal diffusion-limited colloid aggregation. *J. Phys.: Condens. Matter* **1990**, *2*, 3093–3113.
- (34) Lin, M. Y.; Lindsay, H. M.; Weitz, D. A.; et al. Universal reaction-limited colloid aggregation. *Phys. Rev. A: At, Mol, Opt. Phys.* **1990**, *41*, 2005–2020.
- (35) Watzky, M. A.; Finke, R. G. Transition metal nanocluster formation kinetic and mechanistic studies. A new mechanism when hydrogen is the reductant: slow, continuous nucleation and fast autocatalytic surface growth. *J. Am. Chem. Soc.* **1997**, *119*, 10382–10400.
- (36) Bentea, L.; Watzky, M. A.; Finke, R. G. Sigmoidal nucleation and growth curves across nature fit by the Finke-Watzky model of slow continuous nucleation and autocatalytic growth: explicit formulas for the lag and growth times plus other key insights. *J. Phys. Chem. C* **2017**, *121*, 5302–5312.
- (37) LaGrow, A. P.; Ingham, B.; Toney, M. F.; Tilley, R. D. Effect of surfactant concentration and aggregation on the growth kinetics of nickel nanoparticles. *J. Phys. Chem. C* **2013**, *117*, 16709–16718.
- (38) Leo, A.; Hansch, C.; Elkins, D. Partition coefficients and their uses. *Chem. Rev.* **1971**, *71*, 525–616.
- (39) Klier, J.; Tucker, C. J.; Kalantar, T. H.; Green, D. P. Properties and applications of microemulsions. *Adv. Mater.* **2000**, *12*, 1751–1757.
- (40) Kaur, G.; Mehta, S. K. Developments of polysorbate (tween) based microemulsions: Preclinical drug delivery, toxicity and antimicrobial applications. *Int. J. Pharm.* **2017**, *529*, 134–160.
- (41) Pessoa, R. S.; França, E. L.; Ribeiro, E. B.; et al. Microemulsion of babassu oil as a natural product to improve human immune system function. *Drug Des., Dev. Ther.* **2015**, *9*, 21–31.

Recommended by ACS

Enthalpy and Entropy of Scission in Wormlike Micelles

Hanqiu Jiang, Andrew Mulderig, et al.

OCTOBER 23, 2018
LANGMUIR

READ 

Effect of pH on the Structure and Dynamics of Wormlike Micelles in an Amino Acid-Derived Surfactant Composition

Trang Vu, Peter Koenig, et al.

MARCH 31, 2021
LANGMUIR

READ 

Influence of Salt on Supramolecular Oscillatory Structural Forces and Stratification in Micellar Freestanding Films

Subinuer Yilixiati, Vivek Sharma, et al.

JANUARY 09, 2018
ACS NANO

READ 

Influence of the Surfactant Tail Length on the Viscosity of Oppositely Charged Polyelectrolyte/Surfactant Complexes

Giuseppe Rosario Del Sorbo, Emanuel Schneck, et al.

FEBRUARY 12, 2021
MACROMOLECULES

READ 

Get More Suggestions >